Quantum logic control and precision measurements of molecular ions in a ring trap: An approach for testing fundamental symmetries

Yan Zhou[*] and Joshua O. Island
Department of Physics and Astronomy, University of Nevada, Las Vegas, Las Vegas, Nevada 89154, USA

Matt Grau
Department of Physics, Old Dominion University, Norfolk, Virginia 23529, USA

(Received 26 July 2023; revised 26 January 2024; accepted 29 February 2024; published 14 March 2024)

This paper presents an experimental platform designed to facilitate quantum logic control of polar molecular ions in a segmented ring ion trap, paving the way for precision measurements. This approach focuses on achieving near-unity state preparation and detection, as well as long spin-precession coherence. A distinctive aspect lies in separating state preparation and detection conducted in a static frame from parity-selective spin precession in a rotating frame. Moreover, the method is designed to support spatially and temporally coincident measurements on multiple ions prepared in states with different sensitivity to the new physics of interest. This provides powerful techniques to probe and minimize potential sources of systematic error. While the primary focus of this paper is on detecting the electron's electric dipole moment (eEDM) using ^{232}ThF$^+$ ions, the proposed methodology holds promise for broader applications, particularly with ion species that exhibit enhanced sensitivity to the nuclear magnetic quadruple moment (nMQM).

DOI: 10.1103/PhysRevA.109.033107

I. INTRODUCTION

The Standard Model of particle physics stands as a foundational framework for understanding the basic building blocks of matter and their interactions [1,2]. Despite its success, the model leaves many questions unanswered, such as the nature of dark matter and dark energy, the mechanism behind the imbalance of matter and antimatter, and the lack of significant charge and parity (CP) violation in strong interactions [3–8]. One approach to testing the Standard Model involves probing new particles generated in high-energy colliders [9]. Alternatively, tabletop experiments can be conducted using quantum sensors like polar molecules or highly charged ions to detect the dedicated interactions produced by new particles [10–12]. This quantum sensor strategy is conceptually similar to electron-neutron scattering but operates on a much lower energy scale and within tightly bound atomic or molecular systems. In such systems, the probe electron in *s*-type orbitals spends a considerable amount of time in close proximity to and interacting with a heavy nucleus possessing relativistic energy, leading to a subtle but measurable frequency shift in electron spin resonance, which can be detected through precision spectroscopy [13–16].

This paper introduces an approach to measure the electron's electric dipole moment (eEDM) by utilizing quantum logically controlled ^{232}ThF$^+$ ions in a segmented ring ion trap. The quantum logic scheme (QLS) allows for near-unity state preparation and detection [17–21]. The circular motion of ions in the ring trap generates a rotating biased electric field of up to 32 V/cm and supports symmetry-violation searches through spin-precession measurements. To adapt the QLS method and spin-precession metrology, a rotation-induced quantum control scheme is developed to link the QLS procedure in a static frame with a dc magnetic field and the spin precession in a rotating frame with synchronously rotating electric and magnetic fields. This scheme effectively decouples the quantum control and readout of molecular ions from the free evolution of spin precession, thereby facilitating high efficiency in state preparation and detection at an ultracold temperature (∼10 μK) as well as minute-scale spin precession at a moderately high temperature (∼10 K) simultaneously. Furthermore, this platform inherently supports spatially and temporally coincident measurements on multiple ions prepared in states to suppress dominant systematic errors arising from inhomogeneous and time-variant magnetic fields. The proposed method, while incorporating many successful strategies from a well-established experimental platform developed by the Joint Institute for Laboratory Astrophysics (JILA) eEDM group [16,22,23], shifts its focus toward advancing quantum control and readout of single molecules within compact and scalable devices. This strategic refinement is not only aimed at enhancing measurement sensitivity to a sub-μHz accuracy—a level of precision that could uncover new physics at a mass scale above 100 TeV—but also at introducing an alternative methodology, one characterized by its unique set of systematic errors, diversifying the methods available for precision experimentation and analysis. Furthermore, this methodology holds promise for a wide range of molecular species, especially for those with large nuclear spin. These include species like ^{229}ThF$^+$, ^{181}TaO$^+$, and ^{176}LuOH$^+$, known for their enhanced sensitivity to the nuclear magnetic quadrupole moment (nMQM).

---

[*] yan.zhou@unlv.edu

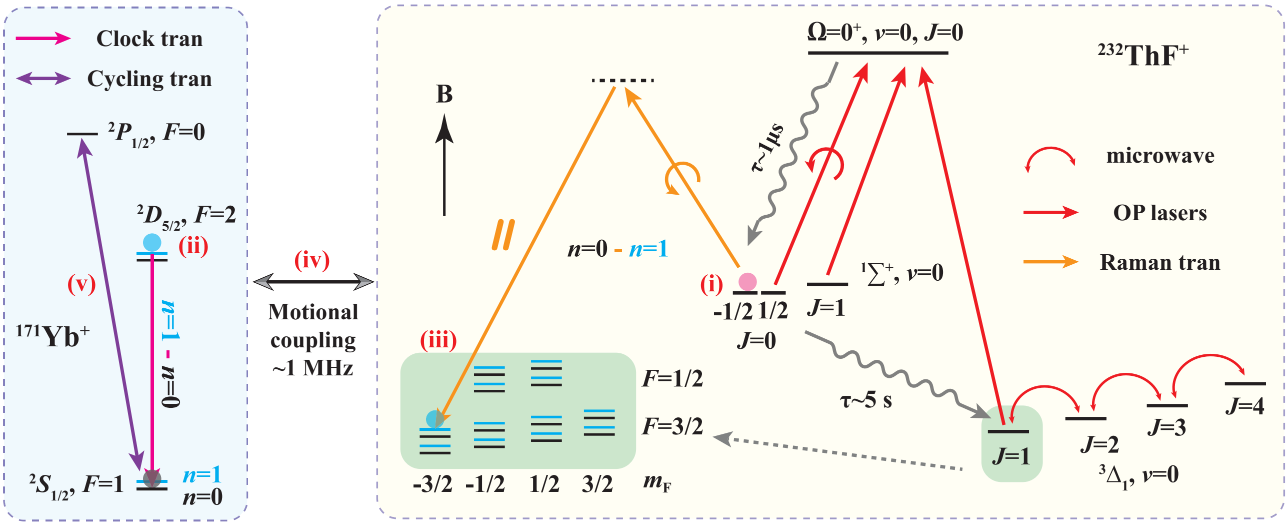

FIG. 1. Experimental scheme of the state preparation using the quantum logic scheme. (a) The schematic diagram of the state preparation of ^{232}ThF$^+$ using OMP and QLS with Yb$^+$. (i) OMP concentrates around 30% population of ^{232}ThF$^+$ in $^1\Sigma^+$, $v = 0, J = 0, m_F = -1/2$ state. Thereafter, (ii) ground state cooling and electron shelving are applied to Yb$^+$, preparing it in $^2D_{5/2}$, $F = 2$, $n = 0$ state, where n labels the motional quantum number of the Yb$^+$ and ^{232}ThF$^+$ ion crystal in the harmonic trap. (iii) QLS transfers ^{232}ThF$^+$ to an eEDM sensitive state, denoted as $^3\Delta_1$, $v = 0, J = 1, m_F = -3/2$, − parity. This is accomplished via a blue sideband of a two-photon Raman transition, which excites one quanta in the collective motional mode of the ^{232}ThF$^+$ and Yb$^+$ ion crystal (iv) [19,21]. The success of this transition, as evidenced by the motional excitation of the Yb$^+$ ion, is detected through an electron shelving process on the narrow $^2S_{1/2}$ to $^2D_{5/2}$ transition, and followed by resonant fluorescence on the $^2S_{1/2}$ to $^2P_{1/2}$ transition (v).

The paper is structured with three critical sections: (1) the preparation of a single, spin-polarized quantum state through the QLS method (as detailed in Sec. II); (2) the implementation of a rotating biased electric field to orient polar molecules (explained in Sec. III); and (3) ensuring the sustainment or generation of maximal spin polarization during the transformation from a static to a rotating frame (discussed in Sec. IV). Furthermore, this paper presents preliminary exploration of practical aspects of the experiment, covering topics like the measurement sequence (Sec. V), systematic uncertainties (Sec. VI), and sensitivity estimations (Sec. VII).

II. STATE PREPARATION AND DETECTION BY QUANTUM LOGIC SCHEME

The $^3\Delta_1$ state of the ^{232}ThF$^+$ molecular ion offers a promising opportunity to improve eEDM measurements, owing to two key factors: (1) the ability to generate an effective electric field of approximately 35 GV/cm, which is 50% larger than that used in the current best electron EDM measurement in HfF$^+$[16], and (2) the potential extended coherence time measurements due to the long lifetime of molecules in the electronic ground state, thereby improving frequency precision. However, the large number of nearly degenerate quantum states poses a challenge, as they dilute the desired coherent signal. The JILA eEDM group has demonstrated approximately 50% state preparation of ^{232}ThF$^+$ in eEDM-sensitive states ($^3\Delta_1$, $v = 0, J = 1$, and single m_F) by employing optical and microwave pumping (OMP) [24]. Moreover, they have developed a rotation-selective resonance-enhanced multiphoton dissociation (REMPD) detection scheme with an efficiency around 30% [25]. The impurity in state preparation stems from population leakage to low-lying electronic states and vibrationally excited states ($v > 1$). The nonideal efficiency of the dissociation detection could be attributed to the complexity of multiple dissociative and radiative channels of the highly excited ^{232}ThF$^+$. To improve the state preparation and detection, substantial spectroscopic work and additional repumping lasers are required. Furthermore, these efforts necessitate repetition and may exhibit significant variation for different molecular species. In this paper, we propose a method that combines OMP and QLS for single quantum state preparation and detection with near-unity efficiency.

Figure 1 illustrates our state-preparation procedure. First, ^{232}ThF$^+$ ions are generated by resonance-enhanced multiphoton ionization (REMPI), by which the population is distributed in a single vibronic state but approximately four rotational states. Second, one ^{232}ThF$^+$ and one Yb$^+$ are loaded into a radio frequency (rf) ion trap at loading zone [trap site 1 in Fig. 2(a)]. The Yb$^+$ ion is Doppler cooled and the ^{232}ThF$^+$ ion is cooled sympathetically. Third, OMP (three microwave frequencies and three continuous wave lasers) transfers approximately 30% of ^{232}ThF$^+$ ions to the $^1\Sigma^+$, $v = 0, J = 0, m_F = -1/2$ state. Spin polarization is generated by a static magnetic field and a circularly polarized pumping laser. Fourth, both ^{232}ThF$^+$ and Yb$^+$ ions are transferred to the QLS zone [trap site 7 in Fig. 2(a)] by modulating the axial trapping potential. Ground state cooling and electron shelving are applied to Yb$^+$, preparing it in the $^2D_{5/2}$, $F = 2$, $n = 0$ state, where n labels the motional state quantum number of the Yb$^+$ and ^{232}ThF$^+$ ion crystal in the harmonic trap. In the axial direction of the ring trap, the motional mode where the two ions oscillate out of phase is utilized as the normal mode here.

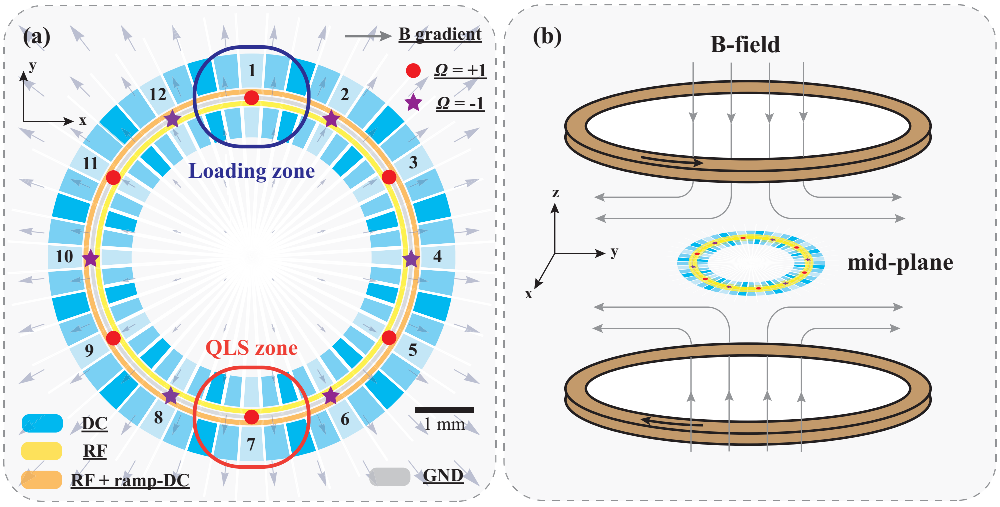

FIG. 2. (a) A schematic diagram displays the segmented ring ion trap used for implementing the QLS scheme and precision metrology with biased electric and magnetic fields. The ions' circular motion generates a rotating electric field and synchronous magnetic field from an applied magnetic field gradient. As the ions initiate their rotation within the ring trap, a ramped dc electric potential is applied on the outer ring electrode, marked in orange, to generate an electrostatic centrifugal field. The amplitude of this ramped electric potential is finely tuned to ensure that the centrifugal force exerted on the rotating ions is primarily derived from this electrostatic field, rather than the rf field. (b) A pair of anti-Helmholtz coils is implemented to generate a linear radial magnetic gradient within the plane of the trap. By reversing the driving current, we can reverse the direction of the magnetic field.

Fifth, a pair of referenced Raman pulses coherently transfer $^{232}\mathrm{ThF}^+$ to one eEDM-sensitive state, such as $^3\Delta_1$, $v = 0$, $J = 1$, $m_\mathrm{F} = -3/2$, $-$ parity. The transition is driven on the blue motional sideband, exciting the collective motional normal mode of the Yb^+ and $^{232}\mathrm{ThF}^+$ ($n = 1$). The m_F selectivity is due to the polarization of the Raman beams and Zeeman detuning. After OMP in the third step, if $^{232}\mathrm{ThF}^+$ is not in the $^1\Sigma^+$, $v = 0$, $J = 0$, $m_\mathrm{F} = -1/2$ state, the motional excitation through the Raman transfer process will not happen, and the normal mode of the ion crystal will still be $n = 0$. Sixth, a blue sideband π pulse ($n = 1 \rightarrow n = 0$) resonantly de-excites the Yb^+ ion's electronic and motional states to $^2S_{1/2}$, $F = 1$, $n = 0$, allowing for cycling fluorescence detection. If the detected photons exceed a threshold, according to the motional entanglement between Yb^+ and $^{232}\mathrm{ThF}^+$, it is nearly certain that the $^{232}\mathrm{ThF}^+$ is at the eEDM-sensitive state. Otherwise, fresh $^{232}\mathrm{ThF}^+$ and Yb^+ ions are loaded (Steps 1 and 2), following which the entire state-preparation procedure is reiterated, starting from the OMP (Step 3) to the QLS detection (Step 6). To specifically target and remove ions from a designated trapping site without affecting the others, radio frequency "tickle" voltage to the dc electrodes resonant with the ion motional frequency. These electrodes, depicted in Fig. 2(a) and detailed in Sec. III, enable precise manipulation by altering the ion's local environment, thus facilitating the selective removal process. This cycle is repeated until the required conditions for state are successfully achieved. Drawing from the greater than 30% OMP efficiency demonstrated by the JILA eEDM group without any vibration repumps [24], on average, we expect to achieve a successful state preparation of $^{232}\mathrm{ThF}^+$ within a few attempts. State detection involves a Raman transfer of $^{232}\mathrm{ThF}^+$ from the $^3\Delta_1$ to $^1\Sigma^+$ state, employing a similar QLS readout method, as described in Step 6. Appendix A contains a preliminary discussion of extending this method to molecules with large nuclear spins.

III. SEGMENTED RING ION TRAP AND ROTATING ELECTRIC AND MAGNETIC FIELDS

Probing T,P-odd symmetry breaks using molecular ions requires the application of a biased electric field to mix states with opposite parities. However, trapped ions are typically incompatible with such electric fields, as even a weak dc electric field (around 10 V/cm) can eject the ions from the trap. The JILA eEDM group first demonstrated polarization of molecular ions using a rapidly rotating electric field [16,22,23]. Implementing QLS in a rotating frame, however, presents challenges due to light delivery complications and excess heating. This paper resolves this conflict by entirely decoupling the QLS and spin precession. A key of the solution involves designing and fabricating a segmented ring trap, as depicted in Fig. 2(a). This trap incorporates several features from a design created by Sandia National Laboratories, which is intended for scalable quantum computation [26].

The ring trap has a radius of 3 mm. The tight radial confinements (~1.5 MHz) are achieved through three concentric rf (20 MHz, 200 $\mathrm{V_{pp}}$) and ground electrodes, while the loose axial confinement (~0.5 MHz) comes from the segmented dc electrodes inside and outside the rf ring electrodes. The trap consists of 96 segmented electrodes divided into 12 groups (+V, 0, −V, 0), forming 12 trapping sites. The trapping sites and ions inside can be rotated clockwise or counterclockwise by modulating the segmented electrodes sinusoidally. Centripetal acceleration provides a rotating electric field that polarizes polar molecules. The maximum amplitude of the electric field (32 V/cm) is determined by the trap radius, maximum rotating frequency (100 kHz), and the mass of the ions. A radial magnetic field gradient, $\mathbf{B} = B'_\mathrm{rad}(2\mathbf{Z} - \mathbf{X} - \mathbf{Y})$, is applied by a pair of anti-Helmholtz coils concentric to the ring trap, as illustrated in Fig. 2(b). As the ions rotate, they also experience a rotating magnetic field ($B_\mathrm{rot} = B'_\mathrm{rad} r_\mathrm{trap}$) that

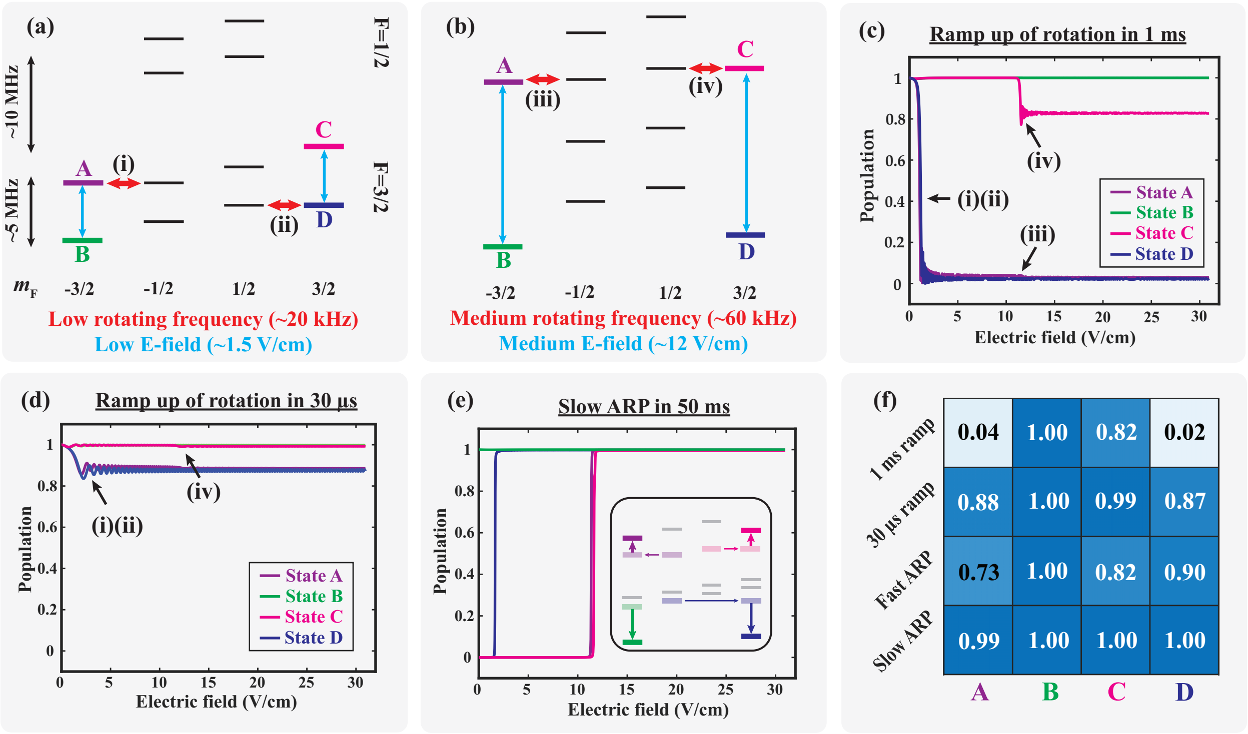

FIG. 3. Spin polarization during the rotating ramp-up procedure. (a and b) Degenerate rotational couplings at low and intermediate electric fields. The light blue arrows mark Stark interactions, and the red arrows mark rotation couplings. (c and d) Numerical evaluations of spin-polarization dynamics with a 1-ms and 30-µs linear ramp, respectively. The arrows mark the population leakage induced by rotational couplings that are indicated in (a) and (b). (e) Numerical evaluations of the spin-polarized state preparation through adiabatic rapid passage (ARP) in 50 ms. Different from States A and C, State D is prepared through a high-order ARP process and State B is initially prepared and kept in the spin-polarized state without the ARP process. (f) Comparison of different rotating ramp-up schemes. The fast and slow ARPs have ramping durations of 1 ms and 50 ms, respectively. Calculation details are described in Appendixes B and C.

is either parallel or antiparallel to the electric field. Reversing the coil current changes the magnetic field direction. When the ions are stationary, although the net electric field is zero, a nonzero static inward or outward magnetic field remains, defining the quantization axis for the QLS scheme of state preparation and detection. In the context of this experimental design, $B_{\rm rot}$ typically ranges from 3 mG to 3 G, which corresponds to Zeeman shifts from 50 Hz to 50 kHz.

To sustain the rotation of ions within the ring trap, a centrifugal force is required. While the radial ponderomotive potential from the rf field could provide this force, excess rf micromotion is detrimental to the preservation of molecular polarization. Specifically, if the maximum 32 V/cm rotating electric field were entirely originated from the time-averaged rf field, the resultant instantaneous electric field would reach several hundred V/cm. Such a strong field would completely depolarize the polar molecules, resulting in an average out of the eEDM contribution. Moreover, this electric field would cause significant heating and rapid ion loss. To address this issue, upon initiating the ions' rotation in the ring trap, we apply a ramped dc electric potential on the outer ring of the trap to generate an electrostatic centrifugal field. We finely tune the amplitude of this ramped potential to ensure that the centrifugal force exerted on the rotating ions predominately comes from the dc field, rather than the rf field. The magnitude of the centrifugal field can be expressed as $E = m\omega^2 r/e$, where m represents the mass of the ions, ω is their angular frequency of rotation, r is the radius of the ion trap, and e is the ion charge. Considering the different masses of the molecular ion ^{232}ThF$^+$ and the logic ion Yb$^+$, it is impossible to provide exact dc centrifugal forces for both species when they rotate at the same frequency within the same trap. Therefore, before initiating rotation, the logic ion Yb$^+$ must be selectively removed or stored in the adjacent trap site. For the ^{232}ThF$^+$ ions alone, it is possible to precisely control the ramped dc electric field within a 1% margin of error. This precision ensures that less than 0.32 V/cm of the centrifugal electric field is attributable to the rf field. With such control, the instantaneous modulating electric field remains at just a few V/cm, thereby preserving the polarization of the molecular ions.

IV. SPIN POLARIZATION AND COHERENT SUPERPOSITION

By integrating QLS, a segmented ring trap, and a static quadrupole magnetic field, we illustrate the state preparation of ^{232}ThF$^+$ in a single spin-polarized eEDM-sensitive state (A, B, C, or D in Fig. 3). Thereafter, the stationary ions will be transferred to a fast-rotating frame, experiencing a net electric field. However, during this transition, the rotation-induced coupling $H_{\rm rot}$ may mix neighboring Zeeman sublevels ($\Delta m_F = \pm 1$) and consequently depopulate the target states [27]:

$$H_{\rm rot} = -\omega_{\rm rot}(F_\parallel \cos\theta - F_\perp \sin\theta), \tag{1}$$

where θ represents the angle between the rotation and quantization axes, ω_{rot} denotes the angular frequency of the rotation, and $F_{\parallel}$ and $F_{\perp}$ are the projections of the total angular momentum operator parallel and perpendicular to the quantization axis, respectively. During the rotation of the ions, although the orientation of the quantization axis undergoes rapid changes, the angle between the rotation axis (aligned along the z direction as shown in Fig. 2) and the quantization axis (situated in the xy plane as shown in Fig. 2) consistently remains at 90°. Therefore, it is only the second term in Eq. (1) that contributes to the rotational coupling in this scenario. However, if the ions exhibit oscillations in the z direction during rotation, it becomes necessary to account for a modulation in the angle θ. The interaction can be strong when the perturbed states ($m_{\mathrm{F}} = \pm 1/2$) become degenerate to the spin-polarized states ($m_{\mathrm{F}} = \pm 3/2$), due to cancellations of Zeeman and Stark shifts at around 1.5 V/cm and cancellations of Stark and hyperfine shifts at around 12 V/cm electric fields, respectively, as indicated by the red arrows in Figs. 3(a) and 3(b). We numerically evaluate the population transfer during the rotating ramp-up induced by such degenerate interactions. Figure 3(c) reveals that the rotational coupling entirely depopulates states A and D, and partially depopulates state C with a 1-ms linear ramp. Only the population of state B remains fully preserved.

To suppress the spin depolarization caused by degenerate interactions, we can increase the rotating ramp rate. Our model shows that a 30-μs ramp duration (3.3 MHz/ms ramp rate) can preserve the spin polarization by approximately 90%, as illustrated in Fig. 3(d). However, applying such a rapidly accelerating field may introduce a detrimental axial electric field or excessive heating or even ion detrapping. A more feasible approach starts with the population in non-spin-polarizing states, and then adiabatically transfers them to the target spin-polarized states through slowly ramped rotation frequency, as depicted in Fig. 3(e). Figure 3(f) summarizes the spin-polarization efficiency after rotation ramp-up using different methods. Through the slow adiabatic rapid passage within 50 ms, nearly 100% populations are prepared in the target states. Calculation details are described in Appendixes B and C.

To initiate and terminate the spin precession, it is crucial to generate effective $\pi/2$ pulses between states A and C, or B and D. Following the approach initiated by the JILA eEDM group, we can establish such coherence by leveraging a fourth-order interaction resulting from combined perturbations of rotational coupling and Stark mixing [23]. An effective two-level Hamiltonian of states A and C, or B and D, can be formulated as

$$H = \begin{bmatrix} -3g_{\mathrm{F}}\mu_{\mathrm{B}}B & p\left(\frac{\omega_{\mathrm{rot}}}{E_{\mathrm{rot}}}\right)^3 \\ p\left(\frac{\omega_{\mathrm{rot}}}{E_{\mathrm{rot}}}\right)^3 & +3g_F\mu_{\mathrm{B}}B \end{bmatrix} = \begin{bmatrix} -3g_F\mu_{\mathrm{B}}B & p'\left(\frac{1}{\omega_{\mathrm{rot}}}\right)^3 \\ p'\left(\frac{1}{\omega_{\mathrm{rot}}}\right)^3 & +3g_{\mathrm{F}}\mu_{\mathrm{B}}B \end{bmatrix}, \tag{2}$$

where g_{F} is the g factor of the $F = 3/2$ state, μ_{B} is the Bohr magneton, B is the amplitude of the effective rotating magnetic field, and all other parameters are grouped in p and p'. The diagonal matrix elements can be manipulated by altering the applied magnetic field gradient, while the off-diagonal matrix elements can be regulated by adjusting the rotating frequency. This enables the generation of off-resonant $\pi/2$ pulses, by modulating either the magnetic field gradient or the rotating frequency. Altering the magnetic field only influences the relative energy shifts of eEDM-sensitive states A and C, or B and D in a range of a few tens of hertz, while ensuring these states are well separated (with over 5 MHz Stark shifts) from the $m_{\mathrm{F}} = \pm 1/2$ states. In contrast, adjusting the rotating frequency can lead to significant changes in the rotating electric field. As depicted in Figures 3(a) and 3(b), any unintended overlap between the eEDM-sensitive states and the $m_{\mathrm{F}} = \pm 1/2$ states would result in a considerable loss of spin polarization. Therefore, modulating the magnetic field is the more favorable approach.

V. EXPERIMENTAL SEQUENCE

Incorporating all the above-described procedures, Fig. 4 illustrates a comprehensive time sequence for the measurements. First, ^{232}ThF$^+$ and Yb$^+$ ions are loaded in the trap. The QLS state preparation scheme is employed to prepare a single quantum state of ^{232}ThF$^+$ within a static magnetic field. To ensure the unity state preparation, multiple cycles of optical pumping, ground state cooling, and QLS readout may be required. The QLS requires that both the molecular ion and the logic ion are in their ground motional state, with the readout process lasting around 1 ms. Therefore, to ensure the high fidelity of this process, the heating rate of the ions in a static trap node must be maintained at less than one motional quantum per millisecond. Once the single quantum state of ^{232}ThF$^+$ is attained, the logic ion Yb$^+$ is subsequently removed. Beginning with this step, the temperature of the ions becomes less of a concern, as the established spin polarization becomes independent of the ions' motion. This detachment ensures that the spin polarization remains stable and intact, unaffected by any subsequent motional excitation of the ions. Second, the ^{232}ThF$^+$ is transported to other trap nodes. It is anticipated that 12 ^{232}ThF$^+$ ions will be prepared within a few seconds. These ions may be prepared in the same quantum state or interleaved in different states to investigate and suppress systematic errors. Third, a slow rotation ramp with a dc centrifugal potential ramp transfers all ions from a static frame to a 100-kHz rotating frame with a 32-V/cm bias electric field. Fourth, the magnetic field amplitude is decreased from 10 gauss to 10 milligauss, followed by abruptly turning the magnetic field off and on for approximately 100 ms to induce coherence (effective $\pi/2$ pulse) between the spin-polarized states. Phase accumulation occurs during an extended spin-precession period in the rotating frame. Subsequently, another $\pi/2$ pulse is applied to map the phase information to the population difference. To achieve high-frequency accuracy, a long phase-evolution time in this step will be pursued, typically ranging from several seconds to a minute. While the spin-precession process does not require maintaining the ions at ultracold temperatures, a significant temperature increase—exceeding 10 K during this phase—could lead to a significant ion loss or induce large amplitude micromotion, both of which are highly undesirable. Therefore, it is crucial to minimize the heating rate while the ions are in the rotating frame. Fifth,

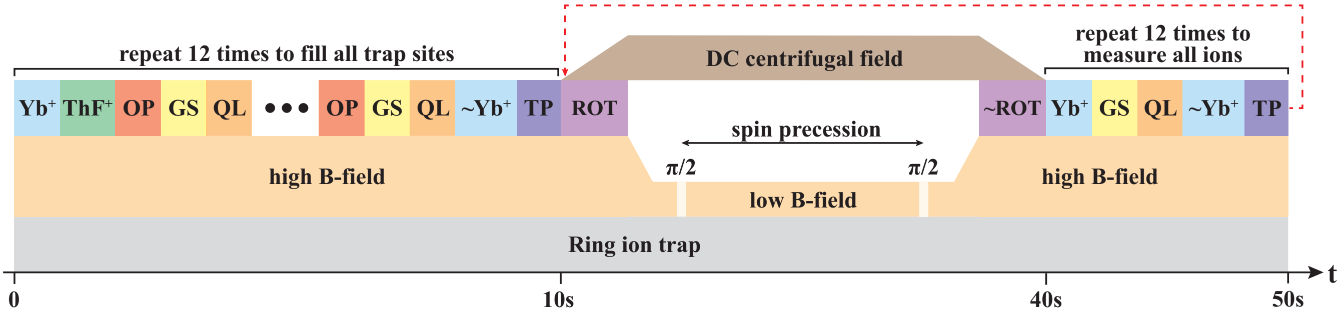

FIG. 4. Time sequence of a single parallelized Ramsey measurement. The abbreviation terms in this plot include Yb^+, ThF^+: creating, trapping, and Doppler cooling Yb^+ and sympathetically cooling $^{232}\mathrm{ThF}^+$; $\sim\mathrm{Yb}^+$: removing Yb^+; OP: optical pumping; GS: ground-state cooling; QL: quantum logic readout; TP: transport the ions from the state preparation site to an adjacent empty site; ROT: ramp up the rotation from 0 to 100 kHz; ∼ROT: ramp down the rotation from 100 kHz to 0. The dashed red arrow indicates the starting point for subsequent measurements. Throughout the entire experimental procedure, the trapping field remains continuously active, the dc centrifugal field is ramped on and off synchronously with the ion rotation, and the modulations of the magnetic field for creating and projecting coherence is implemented during the periods of full-speed rotation.

steps 1–4 are reversed—the magnetic field is ramped up, the rotation frequency is ramped down, and the QLS method is applied to read out states of all 12 ions. In this step, a new logic Yb^+ ion is loaded and utilized to sympathetically cool the $^{232}\mathrm{ThF}^+$ ion back to the ground motional state. Subsequently, the QLS readout method will be applied to detect the quantum state of $^{232}\mathrm{ThF}^+$. Finally, assuming minimal incoherent interactions to the environment after quantum state readout, $^{232}\mathrm{ThF}^+$ should remain in a pure and known quantum state. As a result, subsequent spin-precession measurements can commence immediately without the necessities of state preparation.

VI. SYSTEMATICS

Analysis of systematics is one of the most critical works in the precision measurements, especially in searches for T, P-odd effects, where the anticipated amplitude is often close to zero. In line with the methodologies of the JILA eEDM experiments, three binary switches will be employed: the direction of magnetic field (B switch), the direction of rotation (R switch), and the molecular orientation (D switch) [16,23]. To eliminate prominent systematic terms, a linear combination of eight independent measurements will be utilized [28]. In our experimental scheme, 12 ions within the ring trap will be prepared in different orientations, interweaving with the D switch. Spin-precession measurements, featuring opposite effective electric fields, will be carried out simultaneously in the same device. Such spatially and temporally coincident measurements serve to suppress systematics arising from drifting and inhomogeneous electric and magnetic fields, particularly when the coherence time experiences a significant increase.

In experiments designed to investigate T, P-odd effects, uncontrolled magnetic fields, which cause unexpected phase drifts in spin-precession measurements, represent a major source of systematic error. Furthermore, these phase drifts could also significantly decrease the precision of the frequency extraction, especially when they are large enough to cause deviations from the expected phase condition $\phi_f = (2n+1)\pi/2$. Therefore, precise measurement and control of the magnetic field are critical for the success of these experiments. With the $^{232}\mathrm{ThF}^+$ ion in a rapidly rotating frame, the first-order effects of stray homogeneous magnetic fields are inherently averaged out. Furthermore, a high-frequency ac magnetic field (assuming no induction of parametric oscillations) can also be effectively nullified over the course of a minute-scale spin precession. Thus, the primary magnetic field concern in these experiments becomes the low-frequency magnetic field gradients. To achieve the objective of accurately characterizing the magnetic field gradient within the ring trap, we could use the logic ion Yb^+ as an atomic ion magnetometer. The atomic magnetometers are highly effective for *in situ* assessing the magnetic field either before and/or after or during the spin-precession measurements. Furthermore, these magnetometers could also be positioned in a service trap, which is an integrated part of the ring trap system (though not depicted in Fig. 2), allowing for real-time monitoring and servo control of the magnetic field during the spin-precession measurements. Leveraging the capabilities of a recently demonstrated Ca^+ ion magnetometer, which boasts a sensitivity of 12 $\mathrm{pT/Hz}^{1/2}$ [29], we could significantly reduce the phase uncertainty during the spin-precession process. For instance, in the case of a spin-precession fringe of $^{232}\mathrm{ThF}^+$ observed over 100 s, the phase uncertainty induced by the residual magnetic field gradient is estimated to be only ∼0.2 rad.

Typically, a thorough analysis of systematic errors is undertaken following initial proof-of-principle experiments. However, with the advancements in precise and efficient simulations, many of these systematics could now be accurately reproduced or predicted. Different from the JILA eEDM experiment, which involves thousands of ions, in this paper we work with a single $^{232}\mathrm{ThF}^+$ ion in a trap site. This reduction in complexity makes it feasible to conduct detailed numerical simulations to investigate potential systematic errors without the challenges posed by many-body interactions. By analyzing simulated data, we could proactively identify and address possible issues in the experimental design well before actual experimentation.

TABLE I. Target sensitivities of Generations I, II, and III.

Parameters	Gen. I	Gen. II	Gen. III
Temperature	300 K	4 K	4 K
No. of trap sites (N)	12	12	400
State preparation (P)	90%	95%	95%
State readout (R)	90%	95%	95%
Contrast (C)	90%	95%	95%
Coherence time (τ)	4 s	100 s	100 s
Duty cycle (D)	50%	95%	90%
Data collection (T)	300 h	300 h	1000 h
Frequency precision	39 μHz	5 μHz	0.5 μHz

VII. SCALABILITY AND SENSITIVITY

In contrast to precision measurements employing ensembles of molecules, utilizing a single molecule per trap site compromises the signal readout. To counteract the reduced signal count, it is crucial to develop a scalable ring trap capable of accommodating numerous trap sites. Additionally, the integrated photonic technology pioneered by MIT Lincoln Laboratory may be leveraged to scale light delivery to the trap [30]. As a result, the practical implementation of a large ring trap comprising hundreds of trap sites becomes feasible. Moreover, the absence of high-power pulsed lasers or mechanically moving parts facilitates long-term data acquisition through the incorporation of an autopilot control system.

Table I presents the estimated statistical sensitivities of this scheme. The frequency uncertainty is determined by

$$d\nu = \frac{1}{2\pi C\sqrt{N\tau TDPR}}. \tag{3}$$

The parameters in the above equation are described in Table I. Generation I experiments, conducted at room temperature, could aim to achieve three primary objectives: (1) demonstrate near-unity state preparation and readout schemes utilizing QLS, (2) validate the proposed precision metrology, and (3) conduct an initial investigation of systematic errors. Generation II could be performed at cryogenic temperature to maximize the coherence time through increasing ion trap storage times by improved vacuum in the cryogenic environment, and suppressing rotational and vibrational state changing excitation from black-body radiation. Generation III would focus on implementing highly multiplexed measurements and long data acquisition duration for an ultimate statistical sensitivity. Compared to the leading eEDM measurement by the JILA group using HfF$^+$ with 22.8 μHz sensitivity [16], Generation I would reach a similar level, and Generation III would improve the current best measurement by about two orders of magnitude.

VIII. CONCLUSION AND OUTLOOK

In this paper, we present a design of an experimental platform for T, P-odd measurements, employing quantum logically controlled molecular ions. We detail a road map including quantum state control, precision metrology, and systematic investigations. While our primary focus centers on eEDM measurements using ^{232}ThF$^+$, this scheme could be adapted with minimal strategic alternations to investigate nMQM in other molecular species, such as ^{229}ThF$^+$, ^{181}TaO$^+$, and ^{176}LuOH$^+$.

ACKNOWLEDGMENTS

We thank T. N. Taylor, B. Zygelman, A. Jayich, C. W. Chou, A. Bradley, and R. W. Field for helpful discussions. This work is financially supported by the UNLV Faculty Opportunity Award, NSF RII Track-4 (Grant No. 2327247), and the Virginia Space Grant Consortium.

APPENDIX A: EXTENSION OF QLS METHOD TO MOLECULAR IONS WITH LARGE NUCLEAR SPINS

In Sec. II on state preparation, we employed two methods specific to ^{232}ThF$^+$. The first, rotational-selective REMPI, generates ^{232}ThF$^+$ in approximately four rotational states, which corresponds to a rotational temperature of just a few Kelvin. This fortunate outcome is primarily influenced by the choice of the intermediate states in the REMPI process and the complex pseudo-continuum electronic structures in proximity to the ionization potential. The second technique, OMP, significantly increases the population in the target state. Without OMP, the population in the eEDM-sensitive state (e.g., $^3\Delta_1$, $v=0$, $J=1$, $m_F=-3/2$, $-$ parity) is limited to 2%, compared to 30% with OMP. Although this improvement of more than tenfold is attained using just three lasers and three microwaves, respectively, this level of enhancement might not be reproducible for other molecular species. The unique $\Omega = 0^-$ state of ^{232}ThF$^+$, which only connects to $^3\Delta_1$ and is accessible via visible lasers, enables an efficient OMP process. However, this specific property might be absent in other molecular species. To generalize the experimental platform outlined in this paper for a broader range of molecular species, it is necessary to develop a state preparation scheme that is not contingent on unique properties of specific molecules. In this section, we introduce a preliminary scheme that exclusively employ microwaves. However, comprehensive calculations and evaluations to validate this approach are currently in progress and fall outside the scope of this paper.

Figure 5 illustrates our proposed approach. Initially, we assume that trapped molecular ions are at room temperature, distributed among more than ten rotational states while remaining in a single electronic and vibrational state. To concentrate the population into fewer states, we utilize cryogenic helium gas for sympathetic cooling of the rotational states of molecular ions. At a temperature of 4 K, heavy diatomic molecules like ^{232}ThF$^+$, ^{229}ThF$^+$, and ^{181}TaO$^+$ have approximately 80% of their population in the $^3\Delta_1$, $v=0$, $J=1-3$ states. For molecules with relatively small nuclear spins, such as ^{232}ThF$^+$, there are dozens of sublevels due to hyperfine, Zeeman, and Ω-doubling structures in the first three rotational states. This leads to a 2% chance of a molecule being in an eEDM-sensitive state. Conversely, for molecules with larger nuclear spins, like ^{229}ThF$^+$ and ^{181}TaO$^+$, the number of quantum states for $J = 1$–3 can reach several hundred. Therefore, the probability of achieving a single-state QLS readout drops well below 1%. This low success rate not only prolongs the

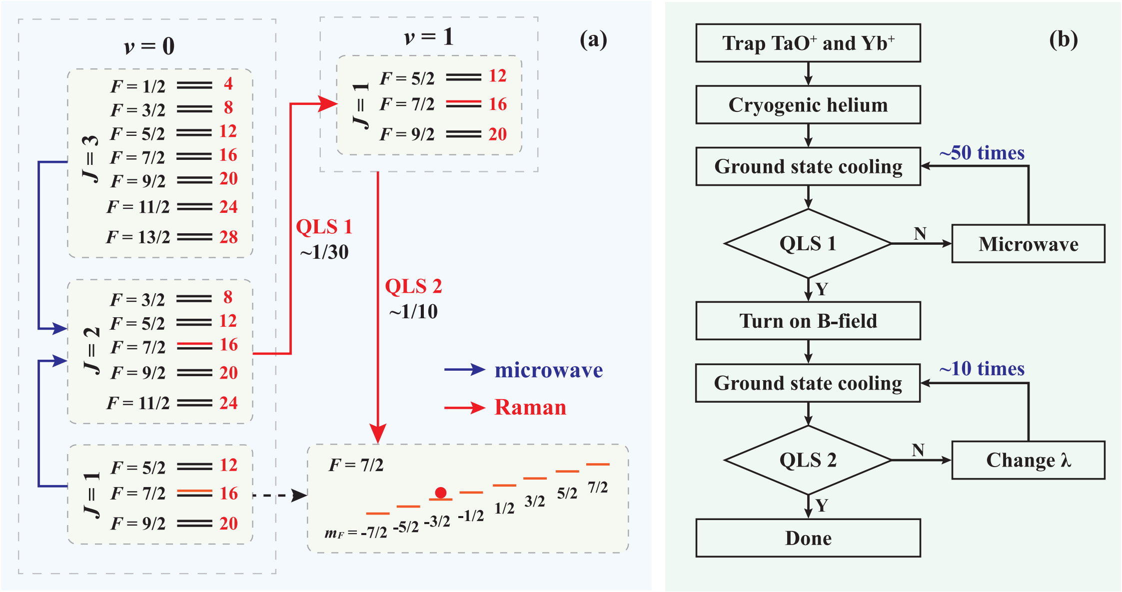

FIG. 5. Schematic diagram of the state preparation scheme using QLS. (a) A two-step QLS approach to prepare a single quantum state of TaO^+, effectively narrowing down from an initial population distribution of 240 states. The red numbers show the value of state degeneracy. (b) A flowchart of the two-step QLS approach.

state preparation time, but also demands a QLS fidelity exceeding 99.9%, a formidable goal.

To streamline the QLS process and minimize the required iterations, we propose a two-step QLS state preparation strategy, as illustrated in Fig. 5(a). The first step of this approach is to perform a QLS transfer from the $v = 0$ states to the $v = 1$ states across several magnetic sublevels. This multiple-state transfer is achievable in a single operation due to degeneracy in the absence of an external magnetic field. A positive QLS readout signals a definitive presence of population within these specific magnetic sublevels with well-known J, F, and parity. Conversely, a negative QLS readout indicates that the initial state at $v = 0$ designated for the QLS measurement is unoccupied. In this case, we apply a microwave π-pulse to transfer populations from other potential states into this initial state. Subsequently, we repeat the QLS transfer to the $v = 1$ states. This process, involving the microwave π-pulse and QLS transfer, might need to be repeated up to 50 times to obtain a positive QLS signal. Following the first step, which concentrates the population from hundreds of states into a few magnetic sublevels, we turn on a magnetic field to lift the degeneracy of these sublevels. Subsequently, we implement the second phase of QLS to transfer the population to one of the eEDM-sensitive states. In this phase, the initial population could be distributed across approximately ten different states. In the least favorable scenario, it becomes necessary to attempt up to ten QLS transfers, each with different Raman transfer laser frequencies. Figure 5(b) presents a flowchart illustrating this two-step procedure.

This method, relying solely on the molecular constants of the ground electronic state, significantly reduces the need for extensive spectroscopy of electronically excited states, thereby making it applicable to a wider range of molecular species. By designing and implementing a dynamic microwave pulse sequence, which is refined using insights derived from prior unsuccessful QLS attempts, it is possible to further reduce the number of iterations required [31]. Although a detailed quantitative analysis is currently underway and beyond the scope of this paper, this method holds promising potential for substantial refinement. Additionally, significant modifications could be explored to adapt this approach for $^{176}\mathrm{LuOH}^+$ and other polyatomic molecules, expanding its applicability further.

APPENDIX B: EFFECTIVE HAMILTONIAN OF $^{232}\mathrm{ThF}^+$ $^3\Delta_1$ STATES

The calculations for spin polarization during the rotation ramp-up process are based on an effective Hamiltonian of the $^3\Delta_1$ state of $^{232}\mathrm{ThF}^+$ [23,32]. The $^3\Delta_1$ state is typically described using Hund's case (a) basis states with coupled nuclear spin,

$$|\Lambda = \pm 2, S = 1, \Sigma = \mp 1, J, \Omega = \pm 1, I = 1/2, F, m_\mathrm{F}\rangle, \tag{B1}$$

where $\Lambda = \mathbf{L} \cdot \mathbf{n}$ is the projection of the electronic orbital angular momentum $\mathbf{L}$ onto the molecular internuclear axis $\mathbf{n}$. The electronic spin angular momentum is represented by $S = |\mathbf{S}|$. The projection of this electronic spin on the molecular internuclear axis is $\Sigma = \mathbf{S} \cdot \mathbf{n}$. $J = |\mathbf{J}| = |\mathbf{L} + \mathbf{S} + \mathbf{R}|$ is the angular momentum, which accounts for electron $(\mathbf{L} + \mathbf{S})$ and molecular rotation $\mathbf{R}$. $\Omega = \mathbf{J} \cdot \mathbf{n}$ is the projection of the total electronic angular momentum $(\mathbf{L} + \mathbf{S})$ onto the molecular internuclear axis. $\mathbf{R}$ does not contribute to Ω because $\mathbf{R} \cdot \mathbf{n} = 0$. The nuclear spin of $^{19}\mathrm{F}$ is denoted by $I = |\mathbf{I}|$, while the nuclear spin of $^{232}\mathrm{Th}$ is zero. $F = |\mathbf{F}| = |\mathbf{J} + \mathbf{I}|$ stands for the total angular momentum, and $m_\mathrm{F} = \mathbf{F} \cdot \mathbf{z}$ represents the projection of this total angular momentum on the rotating quantization axis, which is defined by the electric field. We

TABLE II. Constants used in the effective Hamiltonian of ThF$^+$ and spin-polarization calculations.

Constant	Values	Description
B_e/h	7.293(2) GHz	Rotation constant
$A_\parallel/h$	−20.1(1) MHz	Hyperfine constant
d_{mf}	3.37(9) Debye	Molecule-frame electric dipole moment
$\omega_{\mathrm{ef}}/(2\pi)$	5.29(5) MHz	Ω-doubling constant
$\omega_{\mathrm{rot}}/(2\pi)$	0−100 kHz	Frequency range of the rotating E-field
g_F	0.0149(3)	g-factor of $F = 3/2$ state
r_{trap}	3 mm	Trap radius

define the direction of the molecular internuclear axis **n** as extending from the ^{19}F nucleus toward the ^{232}Th nucleus.

In this paper, our primary objective is to construct a model that accurately captures the dynamics of spin polarization during the rotation ramp-up process. The exigencies of this undertaking are less rigorous compared to the investigations into systematic errors of eEDM. Thus, we streamline our effective Hamiltonian to encapsulate only key interactions of relevance, which comprises the nuclear spin hyperfine interaction, the Stark effect, Ω-doubling, rotation induced m_{F} coupling, and the Zeeman effect:

$$H(\mathbf{E},\mathbf{B},\omega_{\mathrm{rot}}) = H_{\mathrm{hf}} + H_{\mathrm{S}}(\mathbf{E}) + H_\Omega + H_{\mathrm{rot}}(\omega_{\mathrm{rot}}) + H_{\mathrm{Z,e}}(\mathbf{B}) + H_{\mathrm{Z,N}}(\mathbf{B}), \tag{B2}$$

where **E** and **B** denote vector representations of the electric and magnetic fields in the rotating frame, respectively. ω_{rot} is the angular frequency at which the molecular ions circulate within the ring trap. The arrangement of the terms in Eq. (B2) is based on energy scales prevalent under typical experimental conditions. Quantum states that are substantially far off-resonance, such as those relating to excited electronic, vibrational, and rotational states, are omitted from our consideration. Furthermore, we disregard interactions that have negligible impact on the spin-polarization process, such as eEDM.

For each term in Eq. (B2), we first express them in terms of effective operators, and then evaluate the matrix elements of these operators using the Hund's case (a) basis. The nuclear magnetic hyperfine structure from $I = 1/2$ nuclear spin of the Fluorine nucleus is

$$H_{\mathrm{hf}} = A_\parallel(\mathbf{I}\cdot\mathbf{n})(\mathbf{J}\cdot\mathbf{n}) \rightarrow \langle\varphi'|H_{\mathrm{hf}}|\varphi\rangle = \frac{F(F+1) - I(I+1) - J(J+1)}{2J(J+1)} A_\parallel \Omega^2 \delta_{\eta,\eta'}, \tag{B3}$$

where $A_\parallel$ is the hyperfine constant and is listed in Table II. The matrix elements are independent of the Zeeman sublevels (m_{F}) and molecular orientation (the sign of Ω). η represents all other quantum numbers.

The Stark energy shift comes from the interaction between the molecule-frame dipole moment and dc or quasi-dc electric field, which is defined in the laboratory frame. Therefore, spherical tensor algebra is required to connect these frames:

$$H_{\mathrm{S}}(\mathbf{E}) = -\,\mathbf{d}\cdot\mathbf{E} = -\sum_p (-1)^p T_p^{(1)}(\mathbf{d}) T_{-p}^{(1)}(\mathbf{E}) \rightarrow$$

$$\langle\varphi'|H_{\mathrm{S}}|\varphi\rangle = -\,d_{\mathrm{mf}} \sum_{p=-1}^{+1} (-1)^p T_{-p}^{(1)}(\mathbf{E}) (-1)^{F'-m'_{\mathrm{F}}} \begin{pmatrix} F' & 1 & F \\ -m'_F & p & m_{\mathrm{F}} \end{pmatrix} \delta_{I,I'} (-1)^{F+J'+1+I'} \sqrt{(2F'+1)(2F+1)} \begin{Bmatrix} J & F & I' \\ F' & J' & 1 \end{Bmatrix}$$

$$\times \sum_{q=-1}^{+1} (-1)^{J'-\Omega'} \begin{pmatrix} J' & 1 & J \\ -\Omega & q & \Omega \end{pmatrix} \sqrt{(2J'+1)(2J+1)} T_q^{(1)}(\mathbf{n}), \tag{B4}$$

where d_{mf} is the molecule-frame electric dipole moment of the $^3\Delta_1$ state of ^{232}ThF$^+$, which is listed in Table II. $T_p^{(1)}(\mathbf{V})$ is the spherical components of a rank-1 vector operator.

In ^{232}ThF$^+$, the total angular momentum can have two possible orientations or projections along the internuclear axis, designated as $\pm\Omega$. Due to the coupling of the molecule's electronic and rotational angular momentum, these two orientations exhibit a finite energy splitting:

$$H_\Omega = \hbar\omega_{\mathrm{ef}}\Omega_{\mathrm{x}}/2 \rightarrow \langle\varphi'|H_\Omega|\varphi\rangle = \frac{\hbar\omega_{\mathrm{ef}}}{4} J(J+1) \delta_{\Omega',-\Omega} \delta_{\eta',\eta}, \tag{B5}$$

where ω_{ef} is the Ω-doubling constant of the $^3\Delta_1$ state of ^{232}ThF$^+$, which is listed in Table II.

Different from typical Stark spectroscopy with a constant electric field, the experimental scheme in this paper requires a rotating electric field with a frequency from 0 to 100 kHz. Such rotating electric field introduces couplings between states with different m_{F} quantum numbers:

$$H_{\mathrm{rot}} = -\hbar\omega_{\mathrm{rot}} \cdot \mathbf{F} \rightarrow \omega_{\mathrm{rot}} \langle\varphi'|F_{\mathrm{x}}|\varphi\rangle = \frac{\sqrt{2}}{2}(F_+ + F_-) \tag{B6}$$

$$F_\pm = \mp(-1)^{F'-m'_{\mathrm{F}}} \begin{pmatrix} F' & 1 & F \\ -m'_{\mathrm{F}} & \pm1 & m_{\mathrm{F}} \end{pmatrix} \sqrt{F(F+1)(2F+1)} \delta_{J,J'} \delta_{\Omega,\Omega'} \delta_{F,F'} \delta\eta,\, \eta', \tag{B7}$$

where ω_{rot} is the angular frequency of the rotating electric field, whose typical range is listed in Table II.

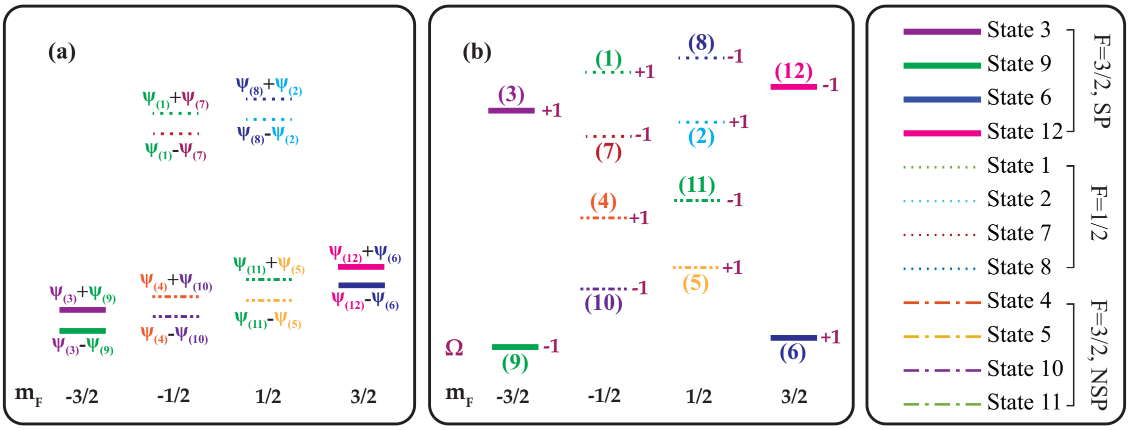

FIG. 6. Depiction of quantum states of ^{232}ThF$^+$, $^3\Delta_1$, $v = 0$, $J = 1$. (a) Qualitative illustration of ^{232}ThF$^+$ situated within a static frame without the presence of an electric field. (b) Qualitative representation of ^{232}ThF$^+$ within a rotating frame subjected to a net electric field. The numbering, line styles, and color schemes associated with each state maintain consistency with those used in Figs. 7–11.

The Zeeman shift comes from two different contributions: (1) electronic [Eq. (B8)] and (2) nuclear spin [Eq. (B9)].

$$H_{\mathrm{Z,e}} = -\mu_{\mathrm{e}} \cdot \mathbf{B} = -\sum_p (-1)^p T_p^{(1)}(\mu_{\mathbf{e}}) T_{-p}^{(1)}(\mathbf{B}) \rightarrow$$

$$\langle\varphi'|H_{\mathrm{Z,e}}|\varphi\rangle = -G_{\parallel}\mu_{\mathrm{B}}\Omega \sum_{p=-1}^{+1} (-1)^p T_{-p}^{(1)}(\mathbf{B})(-1)^{F'-m'_{\mathrm{F}}} \begin{pmatrix} F' & 1 & F \\ -m'_{\mathrm{F}} & p & m_{\mathrm{F}} \end{pmatrix}$$

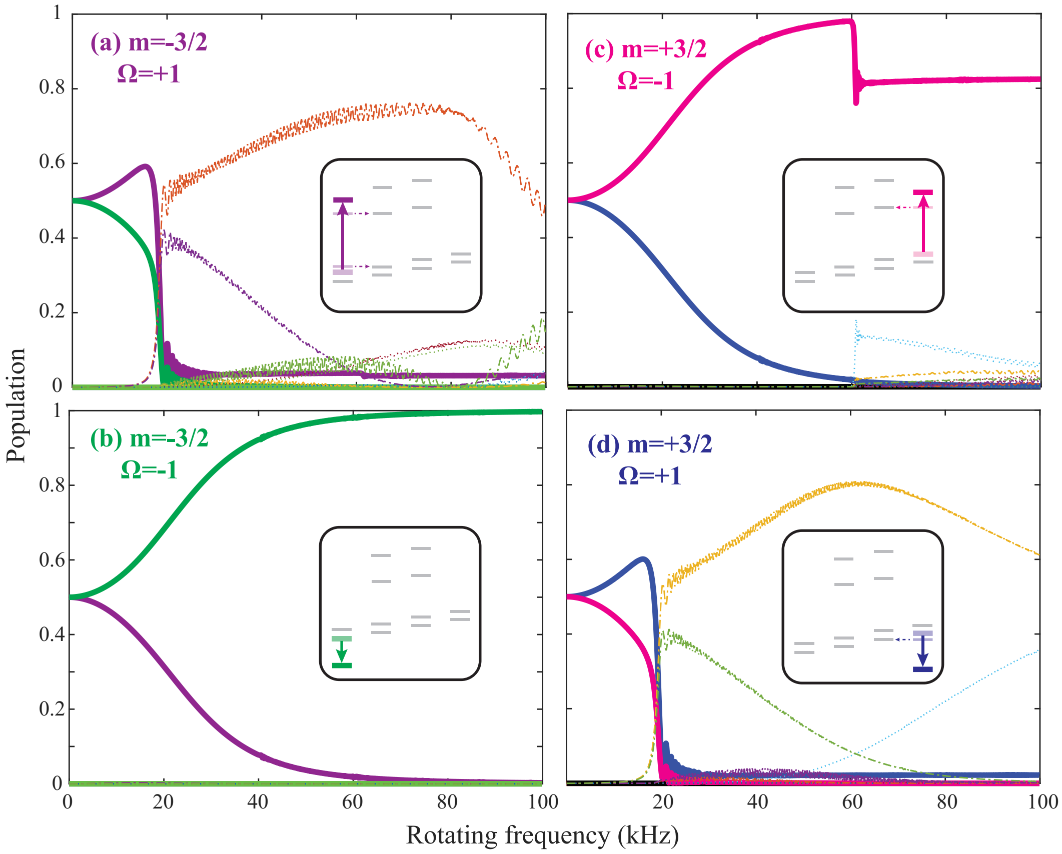

FIG. 7. The evolution of quantum states during a frequency ramp-up in the rotating frame over a span of 1 ms. Significantly, the population in the $m_{\mathrm{F}} = -3/2$, $\Omega = -1$ state emerges as the sole group that can be preserved throughout this procedure. The dashed arrows featured in the inset diagrams illustrate the pathways of population leakage.

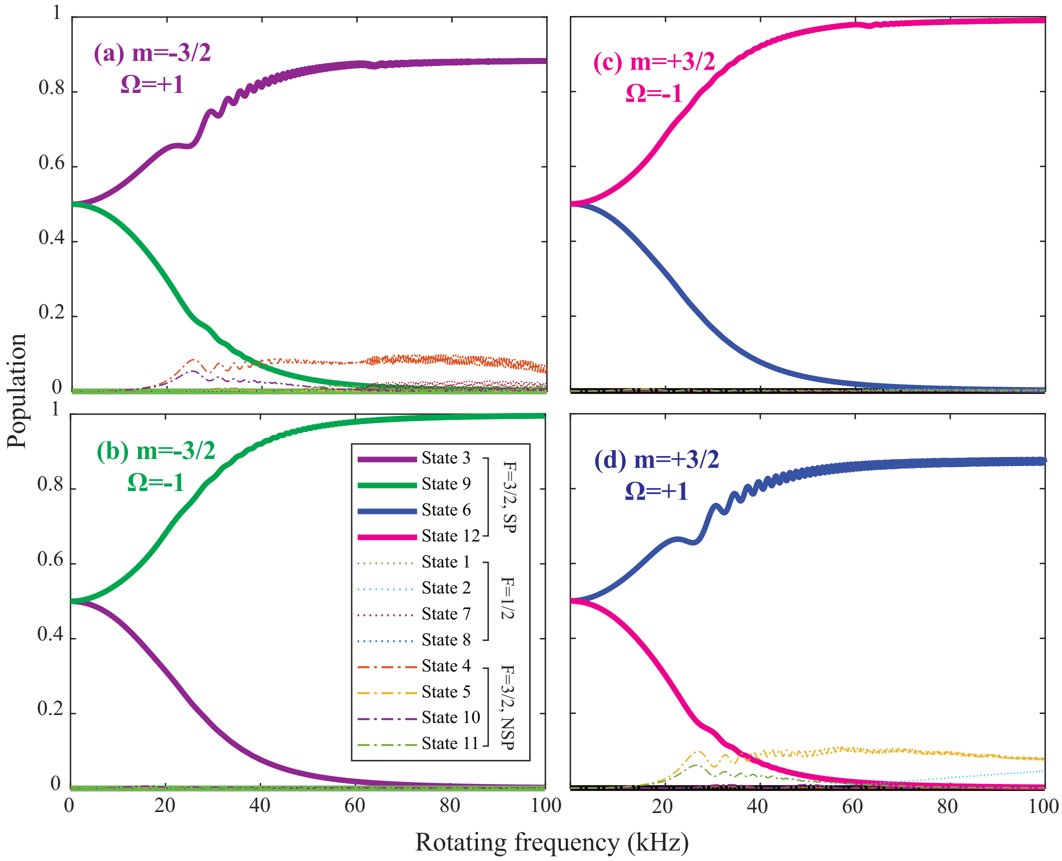

FIG. 8. The evolution of quantum states during a frequency ramp-up in the rotating frame over a span of 30 μs.

$$\times\,\delta_{I,I'}(-1)^{F+J'+1+I'}\sqrt{(2F'+1)(2F+1)}\begin{Bmatrix} J & F & I' \\ F' & J' & 1 \end{Bmatrix}$$

$$\times\sum_{q=-1}^{+1}(-1)^{J'-\Omega'}\begin{pmatrix} J' & 1 & J \\ -\Omega & q & \Omega \end{pmatrix}\sqrt{(2J'+1)(2J+1)}T_q^{(1)}(\mathbf{n}), \tag{B8}$$

$$H_{\rm Z,N} = -\mu_{\rm N}\cdot\mathbf{B} = -\sum_p(-1)^pT_p^{(1)}(\mu_{\rm N})T_{-p}^{(1)}(\mathbf{B}) \rightarrow$$

$$\langle\varphi'|H_{\rm Z,N}|\varphi\rangle = -\sum_{p=-1}^{+1}(-1)^pT_{-p}^{(1)}(\mathbf{B})(-1)^{F'-m'_{\rm F}}\begin{pmatrix} F' & 1 & F \\ -m'_{\rm F} & p & m_{\rm F} \end{pmatrix}$$

$$\times\,\delta_{J,J'}(-1)^{F'+J'+1+I}\sqrt{(2F'+1)(2F+1)}\begin{Bmatrix} I & F & J' \\ F' & I & 1 \end{Bmatrix}\times\sqrt{I(I+1)(2I+1)}g_{\rm N}\mu_{\rm N}. \tag{B9}$$

The parameters $G_\parallel$ and $g_{\rm N}$ signify the strength of the Zeeman interactions. Instead of adopting the theoretical values of these parameters, we use the experimental results from the JILA eEDM group. They have determined an effective magnetic g-factor g_F for the $^3\Delta_1$, $F = 3/2$ states, where the matrices for $H_{\rm Z,e}$ and $H_{\rm Z,N}$ coincide. The g-factor for the $^3\Delta_1$, $F = 1/2$ states should theoretically differ, albeit within the same order of magnitude. However, no experimental measurements have been conducted for these particular states as of now. Given that the uncertainty of the g-factor for these states shows low sensitivity to the quantum control scheme discussed in this paper, we use the same $g_{\rm F}$ for all sublevels of $^3\Delta_1$. This approximation should not introduce significant discrepancies in our quantum control model.

APPENDIX C: RESULTS OF SPIN-POLARIZATION CALCULATIONS

We have investigated various quantum control schemes aimed at the preparation of spin-polarized states in the context of transitioning from a static to a rotating frame. Figure 6 shows the energy diagram of $^3\Delta_1$ states in the static frame with a zero electric field [Fig. 6(a)] and in the rotating frame

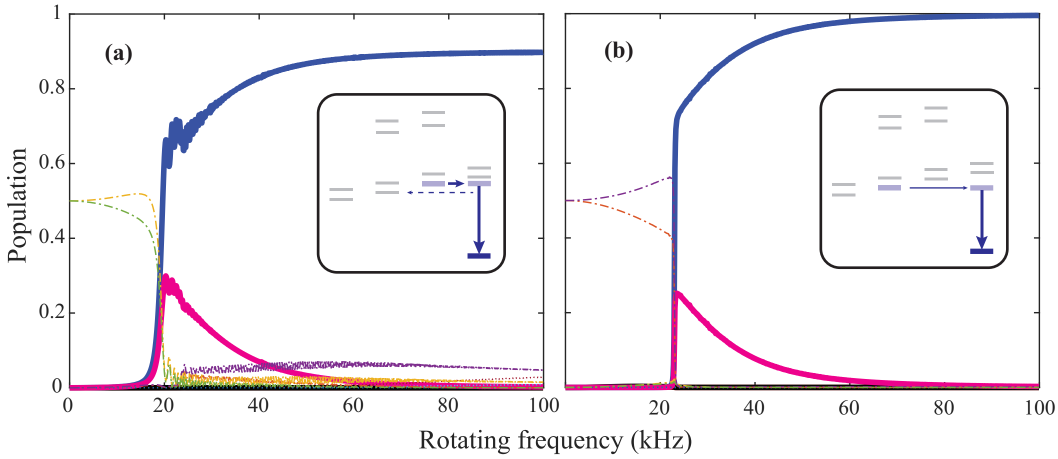

FIG. 9. The preparation of the $m_F = 3/2$, $\Omega = +1$ state via adiabatic population transfer. In (a), the process begins with the $m_F = 1/2$, $F = 3/2$ state through a first-order interaction over a 1-ms rotation ramp-up process. (b) initiates from the $m_F = -1/2$, $F = 3/2$ state and employs a third-order interaction over a 50-ms rotation ramp-up period.

with a net 30-V/cm electric field [Fig. 6(b)]. In the subsequent descriptions, we will employ the molecular orientation Ω as a label for quantum states. It is worth noting that Ω serves as a good quantum number under the condition of a sufficiently large electric field. In the static frame without an electric field, all states become superpositions of $\Omega = \pm 1$.

Figure 7 shows the evolution of quantum states, beginning from spin-polarized states where $m_F = \pm 3/2$, over the course of a 1-ms rotation frequency ramp-up. Notably, only the population of the $m_F = -3/2$, $\Omega = -1$ state remains intact. All other spin-polarized states experience either total or partial population losses to non-spin-polarized states, driven by rotationally induced interactions.

Figure 8 shows the evolution of quantum states from the same initial states as in Fig. 7, but with a much faster frequency ramp-up rate (from 0 to 100 kHz in 30 μs). As we accelerate the ramping rate, there is a substantial decrease in the adiabatic population transfer to non-spin-polarizing states. However, achieving such a high acceleration rate may introduce a detrimental axial electric field or excessive heating or even ion detrapping.

Rather than preparing the spin-polarized quantum state in the static frame, we propose an alternative approach: preparing the non-spin-polarizing state using the QLS method in the static frame. Subsequently, the population can be adiabatically transitioned to the spin-polarized state during the rotating ramp-up process via rotation-induced coupling. Figure 9 demonstrates two strategies for preparing the $m_F = 3/2$, $\Omega = +1$ state via adiabatic population transfer. In Fig. 9(a), we initiate from the $m_F = 1/2$, $F = 3/2$ state and employ a first-order rotation-induced interaction over a 1-ms rotation ramp-up process. Here, we observe that approximately 90% of the population is successfully transferred to the target state. However, around 10% of the population leaks to the $m_F = -1/2$, $F = 3/2$ state through a third-order interaction (indicated by a dashed arrow), which includes one Stark coupling and two rotational couplings. Contrastingly, Fig. 9(b) starts from the $m_F = -1/2$, $F = 3/2$ state and employs a

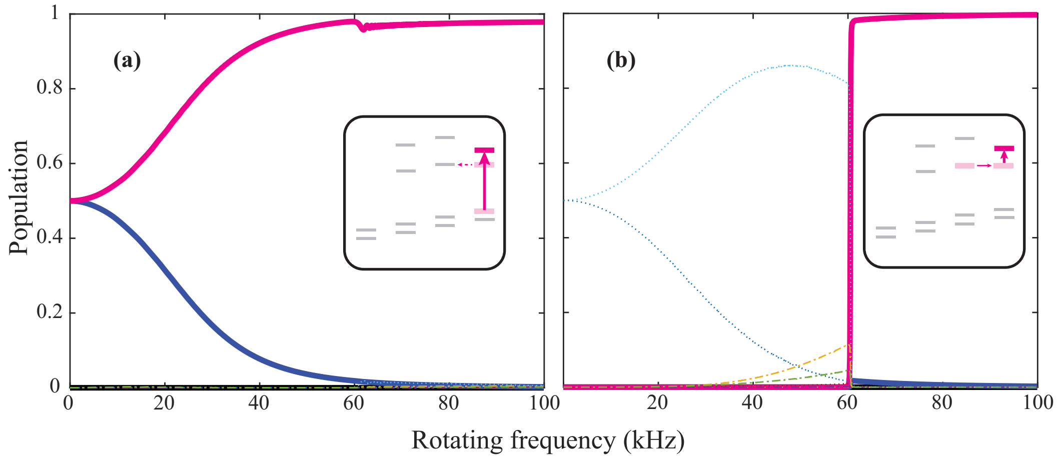

FIG. 10. The preparation of the $m_F = 3/2$, $\Omega = -1$ state. In (a), we start with the spin-polarized $m_F = +3/2$ state and carry out a swift 0.1-ms rotation ramp-up process to circumvent the adiabatic population transfer to the $F = 1/2$ state. (b) initiates the process from the $F = 1/2$ state and employs a 50-ms rotation ramp-up process to achieve the adiabatic population transfer.

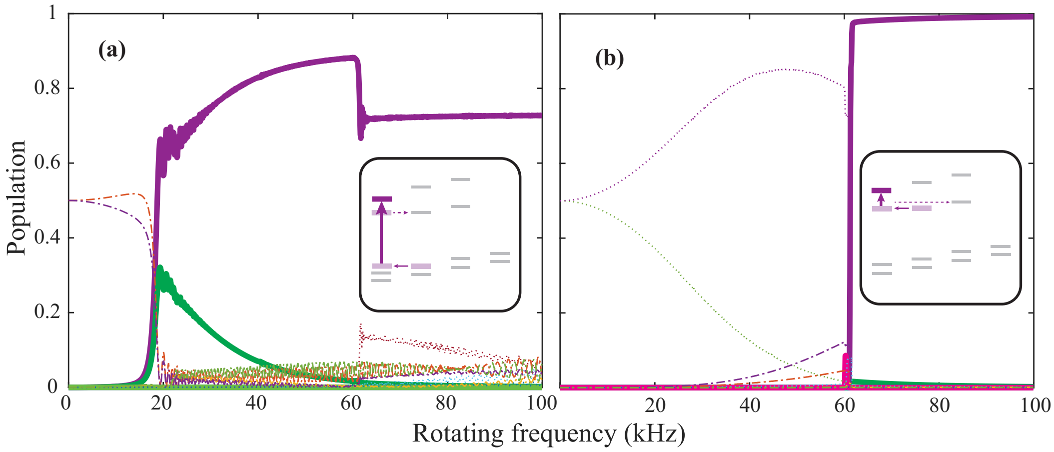

FIG. 11. The preparation of the $m_F = -3/2$, $\Omega = +1$ state. (a) begins with the spin-polarized $F = 3/2$ state and executes a 1-ms rotation ramp-up process to induce the adiabatic population transfer to the $F = 1/2$ state. In contrast, (b) initiates from the $F = 1/2$ state and employs a 50-ms rotation ramp-up process to facilitate adiabatic population transfer.

third-order interaction (indicated by a solid arrow) to transfer the population to the target state. This process requires a significantly slower ramp-up rate of 50 ms. Remarkably, this method enables the achievement of a 100% population transfer to the target state.

In the case of the $m_F = +3/2$, $\Omega = -1$ state, the Stark interaction causes an upward shift in the state, precluding any chance for degenerate interaction with the $m_F = +1/2$, $F = 3/2$ state. However, as the electric field escalates to 12 V/cm at a 60-kHz rotating frequency, population leakage occurs via a relatively weak, yet not insignificant interaction with the $m_F = +1/2$, $F = 1/2$ state. A possible solution to mitigate this leakage is to increase the ramp-up rate (to 0.1 ms ramped-up duration), which can result in a transfer efficiency exceeding 95%, as illustrated in Fig. 10(a). An alternate and potentially more effective approach begins with the $m_F = +1/2$, $F = 1/2$ state and adiabatically transfers the population to the $m_F = +3/2$, $\Omega = -1$ state. As demonstrated in Fig. 10(b), this method can yield a near 100% efficiency.

In the case of the $m_F = -3/2$, $\Omega = +1$ state, we can initiate the process from the $m_F = -1/2$, $F = 3/2$ state as depicted in Fig. 11(a). The population can then be transitioned to the target state via an adiabatic interaction, employing a moderately low ramp-up rate of 1 ms. However, a drawback to this approach is that the population in the $m_F = -3/2$, $\Omega = +1$ state tends to leak to the $F = 1/2$ state through an adiabatic interaction at a 60-kHz rotating frequency. An enhanced strategy involves starting with the $m_F = -1/2$, $F = 1/2$ state, as illustrated in Fig. 11(b). This enables the population to be adiabatically transferred to the target state. Despite this improvement, the population still risks leakage to the $m_F = +1/2$, $F = 1/2$ state via a high-order interaction (indicated by a dashed arrow). Therefore, in this scenario, it becomes necessary to fine-tune the ramp-up rate for the sake of achieving an efficiency of state preparation that approaches unity.

---

[1] G. Hooft, The making of the standard model, Nature (London) **448**, 271 (2007).

[2] P. A. Zyla, R. M. Barnett, J. Beringer, O. Dahl, D. A. Dwyer, D. E. Groom, C. J. Lin, K. S. Lugovsky, E. Pianori, D. J. Robinson, C. G. Wohl, W. M. Yao, K. Agashe, G. Aielli, B. C. Allanach, C. Amsler, M. Antonelli, E. C. Aschenauer, D. M. Asner, H. Baer *et al.*, Review of particle physics, Prog. Theor. Exp. Phys. **2020**, 1 (2020).

[3] J. Engel, M. J. Ramsey-Musolf, and U. Van Kolck, Electric dipole moments of nucleons, nuclei, and atoms: The Standard Model and beyond, Prog. Part. Nucl. Phys. **71**, 21 (2013).

[4] J. L. Feng, Naturalness and the status of supersymmetry, Annu. Rev. Nucl. Part. Sci. **63**, 351 (2013).

[5] D. E. Morrissey and M. J. Ramsey-Musolf, Electroweak baryogenesis, New J. Phys. **14**, 125003 (2012).

[6] J. E. Kim and G. Carosi, Axions and the strong CP problem, Rev. Mod. Phys. **82**, 557 (2010).

[7] M. Trodden, Electroweak baryogenesis, Rev. Mod. Phys. **71**, 1463 (1999).

[8] M. Kobayashi and T. Maskawa, CP-violation in the renormalizable theory of weak interaction, Prog. Theor. Phys. **49**, 652 (1973).

[9] T. Wyatt, High-energy colliders and the rise of the standard model, Nature (London) **448**, 274 (2007).

[10] M. S. Safronova, D. Budker, D. DeMille, D. F. J. Kimball, A. Derevianko, and C. W. Clark, Search for new physics with atoms and molecules, Rev. Mod. Phys. **90**, 025008 (2018).

[11] A. D. Ludlow, M. M. Boyd, J. Ye, E. Peik, and P. O. Schmidt, Optical atomic clocks, Rev. Mod. Phys. **87**, 637 (2015).

[12] M. G. Kozlov, M. S. Safronova, J. R. Crespo López-Urrutia, and P. O. Schmidt, Highly charged ions: Optical clocks and applications in fundamental physics, Rev. Mod. Phys. **90**, 045005 (2018).

[13] V. Andreev, D. G. Ang, D. DeMille, J. M. Doyle, G. Gabrielse, J. Haefner, N. R. Hutzler, Z. Lasner, C. Meisenhelder, B. R.

O'Leary, C. D. Panda, A. D. West, E. P. West, and X. Wu, Improved limit on the electric dipole moment of the electron, Nature (London) **562**, 355 (2018).

[14] R. Alarcon, J. Alexander, V. Anastassopoulos, T. Aoki, R. Baartman, S. Baeßler, L. Bartoszek, D. H. Beck, F. Bedeschi, R. Berger, M. Berz, H. L. Bethlem, T. Bhattacharya, M. Blaskiewicz, T. Blum, T. Bowcock, A. Borschevsky, K. Brown, D. Budker, S. Burdin *et al.*, Electric dipole moments and the search for new physics, Snowmass 2021 (2020), arXiv:2203.08103.

[15] N. R. Hutzler, A. Borschevsky, D. Budker, D. DeMille, V. V. Flambaum, G. Gabrielse, R. F. G. Ruiz, A. M. Jayich, L. A. Orozco, M. Ramsey-Musolf, M. Reece, M. S. Safronova, J. T. Singh, M. R. Tarbutt, and T. Zelevinsky, Searches for new sources of CP violation using molecules as quantum sensors, Snowmass 2021 (2020), arXiv:2010.08709.

[16] T. S. Roussy, L. Caldwell, T. Wright, W. B. Cairncross, Y. Shagam, K. B. Ng, N. Schlossberger, S. Y. Park, A. Wang, J. Ye, and E. A. Cornell, An improved bound on the electron's electric dipole moment, Science **381**, 46 (2023).

[17] C. W. Chou, A. L. Collopy, C. Kurz, Y. Lin, M. E. Harding, P. N. Plessow, T. Fortier, S. Diddams, D. Leibfried, and D. R. Leibrandt, Frequency-comb spectroscopy on pure quantum states of a single molecular ion, Science **367**, 1458 (2020).

[18] P. Micke, T. Leopold, S. A. King, E. Benkler, L. J. Spieß, L. Schmöger, M. Schwarz, J. R. Crespo López-Urrutia, and P. O. Schmidt, Coherent laser spectroscopy of highly charged ions using quantum logic, Nature (London) **578**, 60 (2020).

[19] C. W. Chou, C. Kurz, D. B. Hume, P. N. Plessow, D. R. Leibrandt, and D. Leibfried, Preparation and coherent manipulation of pure quantum states of a single molecular ion, Nature (London) **545**, 203 (2017).

[20] F. Wolf, Y. Wan, J. C. Heip, F. Gebert, C. Shi, and P. O. Schmidt, Non-destructive state detection for quantum logic spectroscopy of molecular ions, Nature (London) **530**, 457 (2016).

[21] P. O. Schmidt, T. Rosenband, C. Langer, W. M. Itano, J. C. Bergquist, and D. J. Wineland, Spectroscopy using quantum logic, Science **309**, 749 (2005).

[22] H. Loh, K. C. Cossel, M. C. Grau, K. K. Ni, E. R. Meyer, J. L. Bohn, J. Ye, and E. A. Cornell, Precision spectroscopy of polarized molecules in an ion trap, Science **342**, 1220 (2013).

[23] W. B. Cairncross, D. N. Gresh, M. Grau, K. C. Cossel, T. S. Roussy, Y. Ni, Y. Zhou, J. Ye, and E. A. Cornell, Precision measurement of the electron's electric dipole moment using trapped molecular ions, Phys. Rev. Lett. **119**, 153001 (2017).

[24] Y. Zhou, Y. Shagam, W. B. Cairncross, K. B. Ng, T. S. Roussy, T. Grogan, K. Boyce, A. Vigil, M. Pettine, T. Zelevinsky, J. Ye, and E. A. Cornell, Second-scale coherence measured at the quantum projection noise limit with hundreds of molecular ions, Phys. Rev. Lett. **124**, 053201 (2020).

[25] K. Ni, H. Loh, M. Grau, K. C. Cossel, J. Ye, and E. A. Cornell, State-specific detection of trapped HfF^+ by photodissociation, J. Mol. Spectrosc. **300**, 12 (2014).

[26] B. Tabakov, F. Benito, M. Blain, C. R. Clark, S. Clark, R. A. Haltli, P. Maunz, J. D. Sterk, C. Tigges, and D. Stick, Assembling a ring-shaped crystal in a microfabricated surface ion trap, Phys. Rev. Appl. **4**, 031001(R) (2015).

[27] E. R. Meyer, A. E. Leanhardt, E. A. Cornell, and J. L. Bohn, Berry-like phases in structured atoms and molecules, Phys. Rev. A **80**, 062110 (2009).

[28] L. Caldwell, T. S. Roussy, T. Wright, W. B. Cairncross, Y. Shagam, K. B. Ng, N. Schlossberger, S. Y. Park, A. Wang, J. Ye, and E. A. Cornell, Systematic and statistical uncertainty evaluation of the formula presented electron electric dipole moment experiment, Phys. Rev. A **108**, 012804 (2023).

[29] T. Ruster, H. Kaufmann, M. A. Luda, V. Kaushal, C. T. Schmiegelow, F. Schmidt-Kaler, and U. G. Poschinger, Entanglement-based dc magnetometry with separated ions, Phys. Rev. X **7**, 031050 (2017).

[30] R. J. Niffenegger, J. Stuart, C. Sorace-Agaskar, D. Kharas, S. Bramhavar, C. D. Bruzewicz, W. Loh, R. T. Maxson, R. McConnell, D. Reens, G. N. West, J. M. Sage, and J. Chiaverini, Integrated multi-wavelength control of an ion qubit, Nature (London) **586**, 538 (2020).

[31] M. Shi, P. F. Herskind, M. Drewsen, and I. L. Chuang, Microwave quantum logic spectroscopy and control of molecular ions, New J. Phys. **15**, 113019 (2013).

[32] K. B. Ng, Y. Zhou, L. Cheng, N. Schlossberger, S. Y. Park, T. S. Roussy, L. Caldwell, Y. Shagam, A. J. Vigil, E. A. Cornell, and J. Ye, Spectroscopy on the electron-electric-dipole-moment-sensitive states of ThF^+, Phys. Rev. A **105**, 022823 (2022).